RSC Advances

ROYAL SOCIETY OF CHEMISTRY

PAPER

View Article Online
View Journal | View Issue

Cite this: *RSC Adv.*, 2026, **16**, 30257

A green approach to water purification: amoxicillin adsorption from aqueous solution by a microwave-synthesized graphene-aminated lignin composite

Riyadh Hossen Bhuiyan, *[a] Md. Masum Billah, [b]
Mohammad Mahbubur Rahman, [a] Swapan Kumer Ray, [a] Monira Binte Mesbah, [c]
Satyajit Roy Rony, [d] Md. Sahadat Hossain, [e] Md. Shohidul Islam, [f]
Md. Kamrul Hasan Dipu, [f] Zahidul Islam[a] and Mohammad Amirul Hoque*[a]

Received 9th March 2026
Accepted 7th May 2026

DOI: 10.1039/d6ra02030e

rsc.li/rsc-advances

This research introduces a new eco-friendly adsorbent, a graphene-aminated lignin (GAL) composite, created through a quick, solvent-free microwave exfoliation method, representing a green and scalable route for advanced adsorbent fabrication. The innovation lies in the integration of defect-minimized graphene with amine-functionalized lignin, enabling enhanced surface functionality, improved dispersion, and abundant active adsorption sites, while polyvinyl alcohol (PVA) was introduced to enhance structural stability and reusability. The composite demonstrated outstanding maximum adsorption capabilities of 96.02 mg g^{-1}, with impressive removal efficiency of 96.02% at an initial concentration of 20 mg L^{-1} under optimal conditions of pH 6, adsorbent dosage of 0.02 g, and reaching equilibrium within 40–60 minutes. The adsorption kinetics followed the pseudo-second-order model, indicating that the process is primarily governed by chemisorption. Isotherm fitting showed excellent agreement with the Langmuir model, suggesting monolayer adsorption on a homogenous surface, while thermodynamic parameters ($\Delta G^\circ = -11.59$; $\Delta H^\circ = 27.53$ kJ mol^{-1}) indicated the process is spontaneous and endothermic. Furthermore, the GAL composite maintained approximately 86.4% efficiency after five reuse cycles, highlighting its potential for regeneration and scalability in real-world wastewater treatment applications. This study presents a sustainable and high-performance adsorbent platform that combines biopolymer valorization with nanomaterial innovation for the advanced removal of pharmaceutical pollutants.

1. Introduction

The growing presence of pharmaceutical pollutants, especially antibiotics like amoxicillin, in water bodies has become a critical environmental and public health concern. Their persistence is attributed mainly to widespread use in both human and veterinary medicine, incomplete metabolic breakdown, and the inability of traditional wastewater treatment systems (WWTSs) to eliminate them effectively.[1] Amoxicillin, a commonly prescribed β-lactam antibiotic, has been detected in surface water, ground water, and even drinking water, often exceeding levels considered environmentally safe, thus contributing to the rise of antimicrobial resistance (AMR).[2] Conventional treatment methods, such as ion exchange, activated sludge processes, membrane bioreactors, and advanced oxidation techniques, frequently fail to entirely remove antibiotic pollutants, resulting in their ongoing release into aquatic ecosystems.[3] These methods are hindered by high energy demands, expensive infrastructure, and the generation of secondary pollutants, making them less suitable for large-scale use.[4] In addition to adsorption-based techniques, electrochemical methods have emerged as highly efficient approaches for the removal of organic pollutants from water due to their strong oxidation capability, environmental compatibility, and ease of operation. Advanced electrochemical processes, particularly electro-Fenton and electrogenerated adsorbents, have demonstrated excellent performance in degrading persistent organic contaminants and antibiotics. For instance, electrocatalytic carbon-based materials have been effectively employed for oxygen reduction reactions and electro-Fenton systems, enabling enhanced degradation of organic pollutants.[5,6] Similarly, electrosynthesized metal hydroxides such as $Mg(OH)_2$ and

---

[a] Fiber and Polymer Research Division, BCSIR Dhaka Laboratories, Bangladesh Council of Scientific and Industrial Research, Bangladesh. E-mail: riyadhbcsir@gmail.com; amirul.bcsir@yahoo.com

[b] Gopalganj Science and Technology University, Gopalganj, Dhaka, Bangladesh

[c] Pilot Plant and Process Development Centre, Bangladesh Council of Scientific and Industrial Research, Dhanmondi, Dhaka, Bangladesh

[d] Pharmaceutical Sciences Research Division, BCSIR Dhaka Laboratories, Bangladesh Council of Scientific and Industrial Research (BCSIR), Dhanmondi, Dhaka-1205, Bangladesh

[e] Institute of Glass & Ceramic Research and Testing (IGCRT), Bangladesh Council of Scientific and Industrial Research (BCSIR), Dhaka-1205, Bangladesh

[f] Department of Chemistry, University of Dhaka, Dhaka-1000, Bangladesh

$Al(OH)_3$ have shown promising adsorption–electrochemical hybrid behavior for the removal of antibiotics and phenolic compounds. Despite their high efficiency, these techniques often involve higher energy consumption, electrode cost, and operational complexity.[7,8] As a result, adsorption-based methods have attracted significant interest owing to their effectiveness, cost-efficiency, and operational simplicity.[9] Although advanced functional materials have been widely explored for environmental applications, particularly in the detection and analysis of metal ions and organic pollutants, nanostructured and hybrid materials, including carbon-based nanomaterials, metal oxides, and composite systems, have demonstrated excellent performance in electrochemical sensing and environmental monitoring due to their high surface area, tunable surface chemistry, and enhanced electron transfer properties.[10,11] Recent studies have reported the effective use of such materials for trace-level detection and removal of heavy metals and contaminants in aqueous systems.[12,13] Despite significant progress in the development of advanced materials for environmental applications, several limitations still hinder their practical implementation. Many nanostructured materials and electrochemical systems, although highly efficient in pollutant detection and removal, often suffer from complex synthesis procedures, high operational costs, and limited scalability. Metal oxide- and carbon-based nanomaterials used in sensing and remediation frequently require sophisticated instrumentation, external energy input, and may involve secondary pollution or poor regeneration efficiency.[14] In addition, issues such as material aggregation, reduced active surface area, and instability in aqueous environments can significantly limit their long-term performance. While electrochemical approaches offer high removal efficiency, they are often energy-intensive and less suitable for large-scale or low-resource applications.

Therefore, there is a growing need for simple, cost-effective, and sustainable materials that can overcome these limitations while maintaining high performance. In this context, the present study develops a graphene–aminated lignin (GAL) composite that integrates the high surface area and conductivity of graphene with the abundant functional groups of a renewable biopolymer. The use of a solvent-free microwave-assisted synthesis provides a rapid, scalable, and environmentally benign fabrication route. Furthermore, the incorporation of aminated lignin enhances adsorption sites and reduces aggregation, while PVA improves structural stability and reusability.[15] Graphene oxide (GO) and few-layer graphene (FLG) show excellent adsorption properties through π–π interactions, hydrogen bonding, and electrostatic interactions with pharmaceutical contaminants.[16] However, their hydrophobic nature, tendency to clump in water, and limited reusability require further modifications to enhance their stability and adsorption efficiency.[17] In this regard, microwave-synthesized graphene has attracted considerable attention as an alternative graphene material due to its rapid, energy-efficient, and scalable production process. Microwave irradiation generates instantaneous volumetric heating and internal pressure within intercalated graphite layers, resulting in rapid exfoliation and the formation of few-layer graphene with expanded surface area and reduced stacking. Compared with conventional chemical oxidation routes, microwave-assisted synthesis can minimize the use of harsh chemicals, shorten processing time, and preserve the intrinsic graphitic structure with fewer basal-plane defects. The resulting graphene sheets generally possess accessible porous morphology and abundant exposed edge sites, which are highly beneficial for adsorption applications. Moreover, defect-rich edge regions and residual oxygen-containing functionalities formed during microwave treatment can provide additional active sites for interaction with antibiotic molecules. These features make microwave graphene a promising platform for developing sustainable, high-performance adsorbents for water purification.[18]

Lignin, a plentiful and renewable biopolymer, shows great potential for boosting the adsorption efficiency of materials based on graphene. Its natural functional groups, such as hydroxyl, carboxyl, and methoxy, enable strong interactions with organic pollutants, especially pharmaceutical contaminants.[19] Research has shown that chemically altering lignin, like through amination or sulfonation, greatly improves its adsorption capacity, selectivity, and recyclability.[20] Combining lignin with graphene materials has been investigated to address aggregation issues while enhancing adsorption kinetics and mechanical stability.[21] This study introduces the synthesis and characterization of a new GAL composite, aimed at overcoming the limitations of traditional adsorbents and improving amoxicillin adsorption performance. The innovation of this method lies in the microwave-assisted exfoliation of graphene, which enables rapid, scalable, and eco-friendly production with fewer structural defects.[22] Furthermore, lignin amination boosts electrostatic interactions with negatively charged pharmaceutical residues, optimizing adsorption selectivity and efficiency. The composite is also crosslinked with polyvinyl alcohol (PVA), which strengthens its structural integrity and enhances reusability.[23] The adsorption performance of GAL was thoroughly assessed through batch experiments, examining key factors such as adsorption kinetics, isotherm models, pH sensitivity, and reusability. In recent years, a variety of biomass-based adsorbents have been explored for their effectiveness in removing AMX and other antibiotics. For example, Ren *et al.* (2020) developed flower-like MnO_2@carbon microspheres (CMn) for the adsorption of AMX from wastewater, which demonstrated a peak adsorption capacity of 16.094 mg g^{-1} at a pH of 7.0, surpassing the performance of biomass carbon microspheres (BCM, 7.424 mg g^{-1}).[24] Aguilar *et al.* reported that the synthesis of hydroxyl-functionalized graphene achieved a maximum adsorption capacity of 59.55 mg g^{-1} at pH 7.[3] Tahmasebi *et al.* synthesized a graphene oxide-gold nanoparticle (GO-AuNPs), which reached a maximum adsorption capacity of 29.2 mg g^{-1} at 323 K and pH 7, achieving equilibrium in 8 hours.[25] The Awad and Jasim developed a graphene oxide/poly(carboxymethyl cellulose-*co*-acrylic acid) (GO/P(CMC-*co*-AA)) hydrogel, which demonstrated a maximum adsorption capacity of 12.486 mg g^{-1} at 298 K and pH 1.2.[2] Zha *et al.* explored AMX adsorption from wastewater using organo-bentonite (DK1) modified with hexadecyl trimethyl ammonium. This method achieved a maximum adsorption capacity of 27.85 mg g^{-1} at 303 K and pH 7.[26] Mohammadi *et al.*

investigated multi-walled carbon nanotubes (MWCNTs), which demonstrated a peak adsorption capacity of 22.9 mg g^{-1}.[27] Previous studies have shown that many reported adsorbents exhibit only moderate adsorption capacities and often suffer from limited reusability, aggregation issues, and insufficient mechanistic understanding. To overcome these limitations, this study presents a GAL composite fabricated through a rapid, solvent-free microwave-assisted exfoliation route. The developed material combines the high surface area and adsorption potential of graphene with the functional diversity and renewability of amine-functionalized lignin, while polyvinyl alcohol (PVA) serves as a crosslinking agent to improve structural integrity and recyclability. This synergistic design enhances dispersion, increases the availability of active adsorption sites, and promotes strong interactions with AMX through electrostatic attraction, hydrogen bonding, and π–π interactions. Compared with previously reported systems, the present work offers an integrated strategy involving green synthesis, biopolymer valorization, rapid adsorption kinetics, high adsorption capacity, and good regeneration performance. Therefore, the GAL composite provides a scalable, cost-effective, and environmentally benign platform for the efficient removal of pharmaceutical contaminants from water.

Furthermore, it lays the groundwork for future studies involving molecular-level adsorption mechanism analysis, real wastewater application, and multi-pollutant removal, thereby contributing to the advancement of next-generation adsorbents for sustainable water treatment.

2. Materials and methods

2.1 Materials

Graphite powder was collected from Loba Chemie, India (98% purity), and ammonium bicarbonate was purchased from Fine Chem Industries, Mumbai. Coconut husk used as the lignin precursor was collected from local sources, thoroughly washed with distilled water to remove dust and impurities, air dried, and subsequently oven-dried at 80 °C to eliminate residual moisture prior to use. Potassium hydroxide (Sigma Aldrich, Germany), hydrochloric acid (Sigma Aldrich, Germany), tetrahydrofuran (Loba Chemie, India), phenol (Merck, Germany), sulfuric acid (Sigma Aldrich, Poland), 1,4-dioxane (Fisher scientific, USA), hexamethylenetetramine (Merck, Germany), formaldehyde (37%) (Merck, Germany), polyvinyl alcohol (Loba Chemie, India), dimethylformamide (Sigma Aldrich, Poland) were procured from standard commercial suppliers and used as received without further purification. Amoxicillin was obtained from a local pharmaceutical supplier. Deionized (DI) water was used throughout all experiments.

2.2 Methods

2.2.1 Synthesis of microwave graphene. Microwave graphene (MG) used in this study was synthesized following our previously reported mechanochemical–microwave exfoliation method.[18] Briefly, graphite was intercalated using ammonium bicarbonate and subsequently exfoliated under microwave irradiation, followed by short thermal annealing to remove residual byproducts. The obtained few-layer graphene exhibited high purity and minimal structural defects and was directly employed for the fabrication of the aminated lignin/graphene composite. Since the synthesis procedure has been described in detail elsewhere, it is not repeated here.

2.2.2 Synthesis of aminated lignin

2.2.2.1 Lignin extraction. Lignin was obtained as black liquor by treating mature coconut husk fibre with a 9% KOH solution at 90 °C for a duration of 3 hours. It was then precipitated in a diluted hydrochloric acid solution with a pH of approximately 3 and subsequently washed with tetrahydrofuran.

2.2.2.2 Lignophenol synthesis. To begin, 7.5 g of lignin was mixed with 30 ml of phenol in a reaction vessel, maintaining a 1 : 4 weight ratio of lignin to phenol. The mixture was stirred at 60 °C using a magnetic stirrer for 30 minutes to form a uniform solution. Next, 4 ml of sulfuric acid (98%) was added as a catalyst to the reaction vessel. The mixture was then stirred magnetically for 240 minutes at 90 °C. After the reaction was complete, the reaction mass underwent vacuum drying at 90 °C. The resulting product was washed with filter paper and distilled water to remove impurities, repeating the process until the solution's pH reached 5.5, as lignin may dissolve at pH levels above 5.5. Finally, to eliminate moisture, the samples were placed in a vacuum oven at 60 °C for 12 hours.

2.2.2.3 Synthesis of aminated lignin from lignophenol. The amination of lignophenol (LP) was carried out using a solution of 1,4-dioxane and water through the Mannich reaction. In this procedure, 1 gram of phenolic lignin was combined with 30 ml of 1,4-dioxane and 10 ml of distilled water in a reaction vessel. The mixture was stirred for 30 minutes to achieve a homogeneous solution. Then, 2 grams of hexamethylenetetramine (99% purity) and 10 ml of 37% formaldehyde were added to the solution, which was then mixed for 4 hours at 90 °C. Following this, the samples were placed in a vacuum oven at 80 °C for 8 hours. Ultimately, the acidified amine-functionalized lignin (Aml) was produced.[28]

2.2.3 Preparation of microwave graphene and aminated lignin composite. To create a composite material made of G and Aml, with PVA acting as a crosslinking agent, a simple solution mixing method was employed. First, 0.7 g of G was dispersed in 20 ml of DMF and stirred for half an hour. Similarly, 0.3 g of Aml was dissolved in 20 ml of DMF and stirred for the same duration. Both solutions were then subjected to sonication for 30 minutes to enhance dispersion. Afterwards, the G and Aml solutions were mixed, and 1–2 wt% PVA was introduced as a crosslinker. The mixture underwent another 30 minute sonication to ensure thorough integration of the PVA. Subsequently, the solution was stirred and centrifuged to remove any undispersed particles. The final composite was dried in a vacuum oven at 60 °C to eliminate any residual solvent.[29]

2.2.4 Characterization. Fourier Transform Infrared Spectroscopy (FT-IR), Thermogravimetric Analysis (TGA), X-ray Diffraction (XRD), and Scanning Electron Microscopy (SEM) were employed to characterize the samples. FT-IR spectra were obtained using a Frontier FT-IR spectrometer (PerkinElmer, UK) in transmittance mode over a wavenumber range of 4000–650 cm^{-1} with a resolution of 4 cm^{-1}. For each measurement, 3 mg of finely powdered sample was mixed with 250 mg of analytical grade KBr and pressed into pellets, with 16 scans collected to improve the signal-to-noise ratio. TGA was carried out using a PerkinElmer thermogravimetric analyzer (PerkinElmer, Waltham, MA, USA), where approximately 5 mg of dried sample was heated from room temperature to 850 °C at a rate of 10 °C min^{-1} under a nitrogen flow of 22 ml min^{-1}, and the resulting weight loss curves were used to evaluate thermal stability and decomposition behavior. XRD (Malvern Panalytical Ltd., UK) analysis was performed using Cu-Kα radiation (λ = 1.5406 Å), scanning over a 2θ range of 10–80° with a step size of 0.01° at a rate of 0.05° s^{-1} under operating conditions of 40 kV and 50 mA, to examine crystallographic properties and interlayer spacing. Surface morphology was further studied by SEM (EV018, Carl Zeiss AG, Germany); samples were mounted on carbon tape, sputter-coated with platinum to prevent charging, and imaged at varying magnifications under high vacuum to investigate surface features and microstructural characteristics. UV-Vis spectroscopy of solid samples was performed using a PerkinElmer Lambda 365 UV-Vis spectrophotometer. For each measurement, 17 mg of sample was thoroughly mixed with 308 mg of analytical-grade KBr, pressed into pellets, and scanned over the UV-Vis range (200–800) to analyze optical absorption characteristics and estimate band gap energies.

2.2.5 Adsorption analysis. In the batch adsorption experiments, an AMX solution was placed in a beaker, and the adsorbent, a GAL composite, was added at room temperature. The filtrates were then examined using UV-Vis spectroscopy (PerkinElmer Lambda 365) to assess adsorption performance under different process conditions. The study explored initial AMX concentrations ranging from 5 to 20 mg L^{-1} over a period of 0 to 120 minutes, with a pH range of 2 to 10 at the optimal contact time, and adsorbent dosages between 0.01 and 0.035 g at the optimal contact time and pH 5. The adsorption capacity (Q_e) and removal efficiency were determined as follows:

$$Q_e = \frac{C_i - C_e}{M} \times V \tag{1}$$

$$\text{Removal efficiency} = \frac{C_i - C_e}{C_i} \times 100 \tag{2}$$

where C_i and C_e (mg L^{-1}) are the initial and final AMX concentrations, V (L) is the solution volume, and M (g) is the mass of the adsorbent.[30]

2.2.6 Adsorption kinetics. To elucidate the adsorption mechanism, multiple kinetic models, namely the pseudo-first-order, pseudo-second-order, and intra-particle diffusion models, were applied to the experimental data. The mathematical expressions for these models are provided in eqn (3)–(5):

Pseudo-first order kinetic model:

$$\ln(Q_e - Q_t) = \ln Q_e - K_1 t \tag{3}$$

Pseudo-second order kinetic model:

$$\frac{t}{Q_t} = \frac{1}{K_2 {Q_e}^2} + \frac{t}{Q_e} \tag{4}$$

Intra-particle diffusion model:

$$Q_t = K_{\text{diff}} \times t^{1/2} + C \tag{5}$$

where, Q_t and Q_e denote the adsorption quantities (mg g^{-1}) at time t (min) and at equilibrium, respectively, K_1 (min^{-1}), K_2 (g (mg min)$^{-1}$), and K_{diff} (mg (g min$^{1/2}$)$^{-1}$) represent the rate constants associated with pseudo-first-order, pseudo-second-order, and intra-particle diffusion, respectively, C denotes the thickness of the boundary layer.[30]

2.2.7 Adsorption isotherm. To evaluate the equilibrium adsorption characteristics and the interaction between AMX and GAL composite, the study applied the Langmuir, the Freundlich, and the Temkin isotherm models. These models offer insights into adsorption behavior, surface interactions, and energy distribution. The linear forms of these adsorption isotherms used in the study are outlined below:

Langmuir isotherm equation:

$$C_e Q_e = \frac{1}{Q_m K_L} + C_e Q_m \tag{6}$$

Freundlich isotherm equation:

$$\ln Q_e = \ln K_F + \frac{1}{n} \ln C_e \tag{7}$$

Temkin isotherm equation:

$$Q_e = B \ln K_t + B \ln C_e \tag{8}$$

where Q_m signifies the maximum adsorption capacity of AMX on the adsorbents (mg g^{-1}), K_L is the Langmuir constant (L mg^{-1}), K_F is the Freundlich constant [(mg g^{-1}) (L mg^{-1})$^{1/n}$], K_t is the equilibrium binding constant, n represents the adsorption intensity constant, and B is related to the adsorption heat.[30]

2.2.8 Reusability. The potential for reusing GAL adsorbents was assessed through repeated adsorption and desorption processes. Optimal conditions for AMX adsorption were found at a pH of 6, with a duration of 1 to 2 hours, followed by separating the solid and liquid phases through filtration. Desorption was carried out using HCl solutions ranging from 0.1 to 1 M, with continuous stirring for an hour. After desorption, the adsorbents were thoroughly washed with deionized water until a neutral pH was reached, then dried at 60 °C to regain their adsorption capacity. This process was repeated until the adsorption efficiency dropped below 80%, setting a practical limit for sustainable use in water treatment applications.[31]

3. Results and discussion

3.1 FTIR analysis

Fig. 1 shows the FT-IR spectrum of the GAL composite, along with its components. The spectrum reveals distinct shifts and

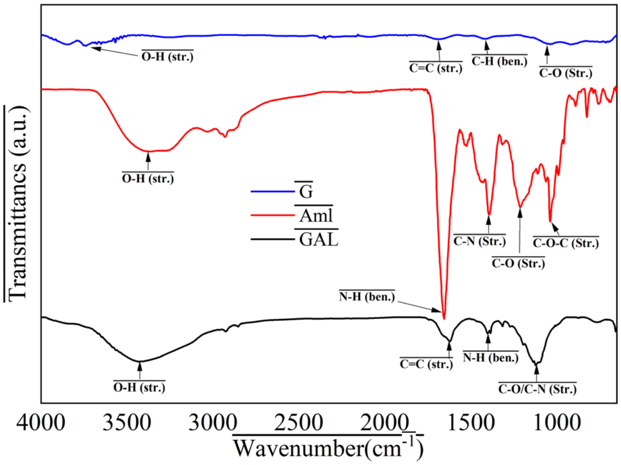

Fig. 1 FTIR spectra of G, Aml, and GAL composite.

intensity variations that confirm molecular interactions between graphene and aminated lignin. For graphene, the weak and broad band observed around 3400 cm^{-1} is attributed to O–H stretching vibrations arising from adsorbed moisture and residual hydroxyl groups on defect sites. The peaks near 1620 cm^{-1} correspond to skeletal vibrations of aromatic C=C bonds within the graphitic framework, while bands in the region of 1400 and 1050 cm^{-1} are associated with residual C–H and C–O stretching of oxygen-containing surface functionalities.[18] The spectrum of Aml exhibits a broad and intense absorption band centered at 3250–3450 cm^{-1}, assigned to overlapping O–H and N–H stretching vibrations, indicating the presence of hydroxyl and introduced amine groups after lignin amination.[32] The peaks located at 2920 and 2850 cm^{-1} are attributed to asymmetric and symmetric C–H stretching vibrations of aliphatic –CH_2/–CH_3 groups. A strong band around 1600 cm^{-1} corresponds to aromatic ring skeletal vibrations (C=C) combined with N–H bending, which is characteristic of lignin-derived aromatic structures.[33]. The peak near 1510 cm^{-1} is associated with aromatic ring vibrations of the guaiacyl/syringyl units of lignin. The absorption band around 1450–1420 cm^{-1} is assigned to C–H deformation and methoxy group vibrations. The band near 1320–1260 cm^{-1} is attributed to C–N stretching and aromatic C–O vibrations, confirming successful amination of lignin. In addition, the strong peaks at 1120–1036 cm^{-1} are assigned to C–O stretching of primary alcohols, ethers, and phenolic groups present in the lignin backbone.[32]. After composite formation, the GAL spectrum retains the major functional features of both graphene and aminated lignin but with noticeable shifts and intensity changes, confirming successful integration. The broad O–H/N–H band becomes less intense and slightly shifted, indicating hydrogen bonding interactions between hydroxyl/amine groups of Aml and oxygenated sites of graphene.[34] The aromatic C=C band around 1600 cm^{-1} becomes broadened, suggesting π–π stacking interactions between the aromatic domains of lignin and graphene sheets. The decreased intensity and slight shift of peaks in the 1260–1036 cm^{-1} region indicate involvement of C–O and C–N groups in interfacial bonding.[35] These spectral changes confirm that the GAL composite was formed through synergistic interactions including hydrogen bonding, π–π interactions, and possible electrostatic attraction rather than simple physical mixing. Such surface functionalization is expected to enhance active site availability and improve adsorption affinity toward amoxicillin molecules.[36].

3.2 TGA analysis

The thermal stability of G, Aml, and their composite (GAL) was assessed using TGA in a nitrogen atmosphere, as depicted in Fig. 2. The TGA curves reveal distinct thermal degradation patterns for each material, reflecting their inherent thermal properties and interactions within the composite. G showed exceptional thermal stability, maintaining over 95% of its original weight up to around 600 °C. The minimal weight loss below 150 °C suggests a low presence of moisture or volatile substances. This remarkable thermal resistance is typical of graphitic materials due to their stable conjugated carbon structure.[37] Conversely, Aml begins to experience significant weight reduction starting at approximately 200 °C, which persists until 400 °C. This pattern is characteristic of lignin due to the breakdown of its hemicellulose and cellulose components.[38] These elements are thermally unstable, leading to considerable volatilization of moisture and organic compounds when heated.[39] The pronounced decrease in mass, especially between 300 °C and 500 °C, is linked to the degradation of lignin's intricate structure, which is less stable compared to carbon-based materials like graphene.[40] The GAL exhibits thermal behavior that is intermediate between G and Aml. Initially, the GAL composite shows weight loss akin to AL, beginning around 200 °C, but at a noticeably slower pace. This is attributed to the presence of G, which serves as a thermal stabilizer for lignin, thereby slowing down its decomposition rate. The reduced rate of weight loss in GAL suggests that graphene is shielding the lignin from rapid degradation, and the high stability of graphene enhances the thermal resistance of the composite material. Unlike AL, the GAL composite retains more weight at temperatures exceeding 400 °C, indicating that graphene boosts the thermal stability of the composite. The retention of mass at temperatures up to 800 °C further underscores graphene's role in enhancing the overall thermal properties of lignin-based materials. This aligns with studies where graphene has been shown to decelerate the decomposition of organic polymers by reinforcing their structure.[40]

3.3 SEM analysis

Fig. 3 shows the SEM image of G, Aml, and GAL composite that reveals the surface morphology of these materials. The SEM image of the GAL composite offers an in-depth look at the microstructural features and interactions between its components. Graphene is mainly seen as a crumpled, flat surface and overlapping sheets, which align with its natural structure. The crumpled form of the graphene sheets in the composite may increase the surface area available for interactions, making it beneficial for applications that require high conductivity and

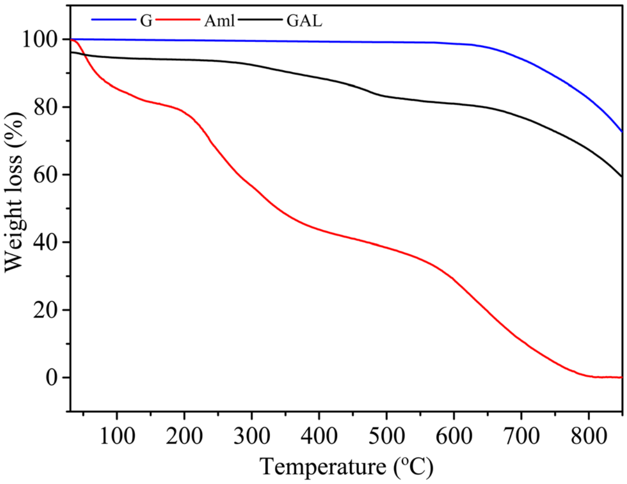

Fig. 2 TGA curve of G, Aml, and GAL composite.

structural reinforcement.[41] Conversely, the Aml particles display a more irregular and porous structure. Additionally, it has a rough, granular texture, which can be attributed to the functionalization of lignin with amine groups. This modification enhances its chemical reactivity, allowing for stronger interaction with graphene, thereby improving the dispersion and bonding between the two materials.[40] The observed interaction between the G sheets and Aml particles suggests a synergistic effect within the composite material, and surface texture will likely be G sheets embedded within the fibrous Aml network, forming a microstructure that enhances surface area.[42]

3.4 XRD analysis

Fig. 4 represents the XRD patterns of three distinct materials: G, Aml, and their composite, GAL. The XRD pattern for G (blue line) reveals two notable peaks, which are typically seen in graphitic structure. The central peak near $2\theta = 26.5°$ corresponds to the (002) plane, indicating the interlayer spacing between graphene sheets. This sharp peak signifies a well-ordered crystalline structure in the graphene. Additionally, a secondary peak at $2\theta = 54°$, associated with the (004) plane, is also present, further confirming the crystalline nature of the graphene material. The presence of both the (002) and (004) planes suggests a relatively high degree of structural order within the graphene sheets, as these peaks are characteristic of graphene's hexagonal lattice structure.[43] In contrast, the XRD pattern of Aml (red line) displays a broad and diffuse peak around $2\theta = 20–30°$, indicative of its amorphous nature. This broad peak is typical of lignin, as it lacks a well-defined crystalline structure, indicating that the material remains disordered mainly at the atomic level.[44] When examining the XRD pattern of the GAL (black line), it shows a combination of both crystalline and amorphous characteristics. The composite retains the sharp peak around $2\theta = 26.7°$ (from the graphene's (002) plane), despite it might be slightly shifted or broadened,

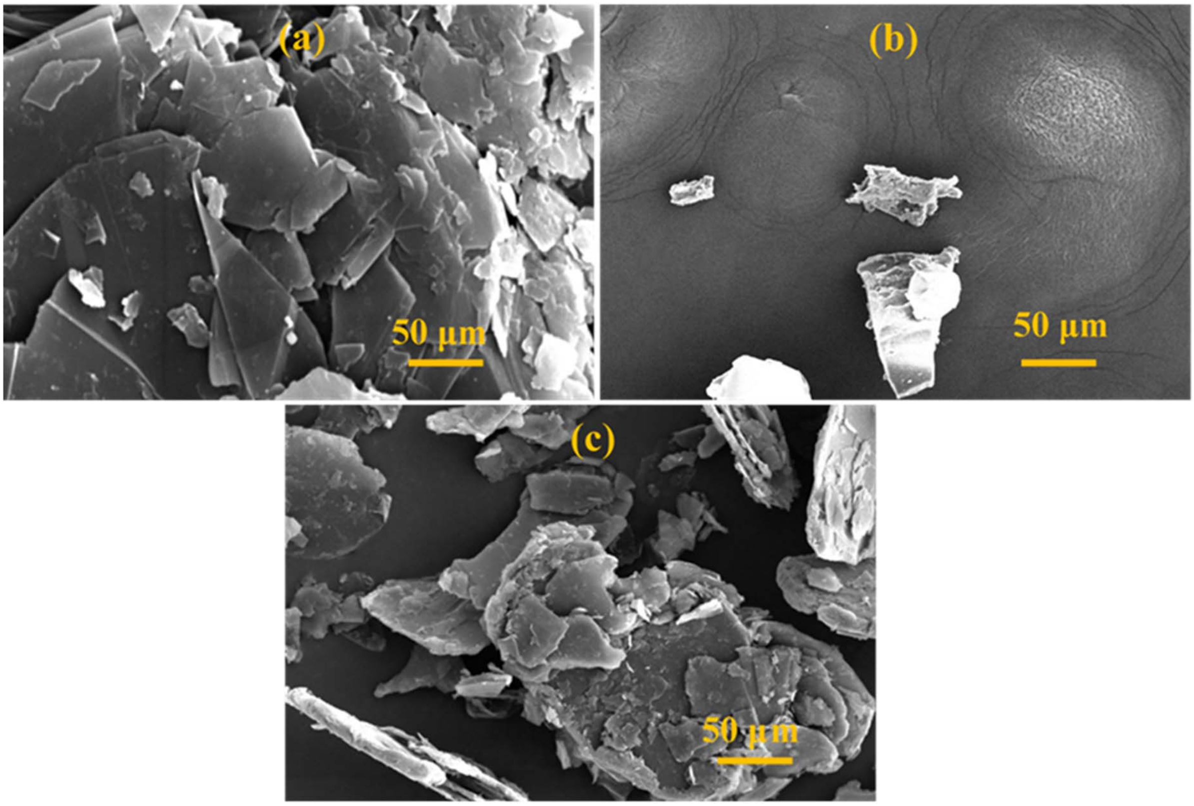

Fig. 3 SEM image of (a) G, (b) Aml, and (c) GAL composite.

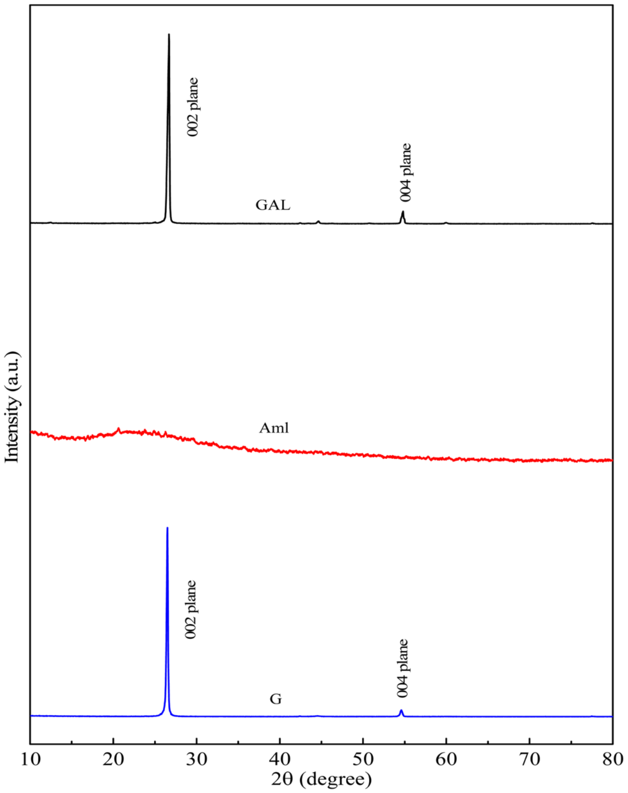

Fig. 4 XRD pattern of G, Aml, and GAL composite.

due to changes in the interlayer spacing or interactions at the molecular level.[45]

The interlayer spacing (*d*-spacing) was calculated using Bragg's law:

$$n\lambda = 2d\sin\theta$$

The calculated *d*-spacing for the (002) plane was found to be approximately 0.334 nm, which is consistent with typical graphitic structures, indicating that the fundamental layered structure of graphene is preserved in the composite.[18]

Furthermore, the crystallite size of the GAL composite was estimated using the Scherrer equation:

$$D = \frac{K\lambda}{\beta\cos\theta}$$

where D is the crystallite size, K is the shape factor (0.9), λ is the X-ray wavelength (1.5406 Å), β is the full width at half maximum (FWHM), and θ is the Bragg angle. The calculated crystallite size was approximately 31 nm, confirming the formation of nanoscale graphene domains.[18] The reduced crystallite size and peak broadening indicate the successful incorporation of aminated lignin, which disrupts graphene stacking and enhances surface area.

3.5 UV-Vis spectroscopy analysis

UV-Vis absorption spectra of G, Aml, and GAL composites are presented in Fig. 5. G exhibited a characteristic absorption maximum at 270 nm, corresponding to the π–π* transition of aromatic C=C bonds.[46] Aml displayed a prominent peak at 285 nm, assigned to the π–π* transitions of phenolic aromatic structures.[47] Upon composite formation (GAL), the maximum absorption peak was slightly shifted to 274 nm with reduced intensity, indicating electronic interactions between G sheets and Aml moieties.[48] This bathochromic shift and suppression of absorbance suggest π–π stacking and hydrogen bonding, confirming the successful integration of GAL composite.

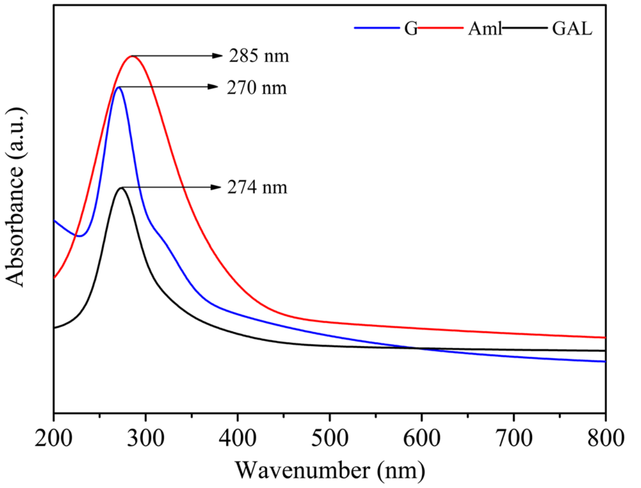

Fig. 5 UV-Vis spectra of G, Aml, and GAL composite.

Fig. 6 illustrates the band gap energies of G, Aml, and GAL composite. The low band gap of G (0.97 eV) is consistent with its semimetallic nature, where residual defects and edge effects induced during microwave exfoliation contribute to opening a finite gap.[49] In contrast, Aml shows a much wider band gap (2.49 eV), reflecting the non-conjugated aromatic structure and electron localization of lignin macromolecules.[50] Interestingly, upon composite formation, the GAL hybrid exhibits a marginal increase in band gap (2.58 eV) compared to Aml. This slight widening can be attributed to electronic interactions and charge transfer between G Sheets and lignin's aromatic/amine groups, leading to modified energy states and suppressed localized defect levels. The result implies that the composite possesses a more ordered interfacial electronic environment, which may enhance stability, exciton confinement, and optoelectronic response. Such band gap modulation has been observed in other carbon-biopolymer composites, where π–π stacking and hydrogen bonding tune optical transitions and electronic structure.[50]

The band gap analysis of the synthesized composite indicates a moderate increase in band gap compared to its individual components, suggesting improved electronic order and reduced defect-induced recombination. This wider band gap plays a crucial role in enhancing adsorption performance toward AMX by promoting stronger interactions between surface functional groups and antibiotic molecules. The increased band gap is associated with a higher density of oxygen- and nitrogen-containing moieties, improved surface polarity, and enhanced hydrogen-bonding capacity, all of which

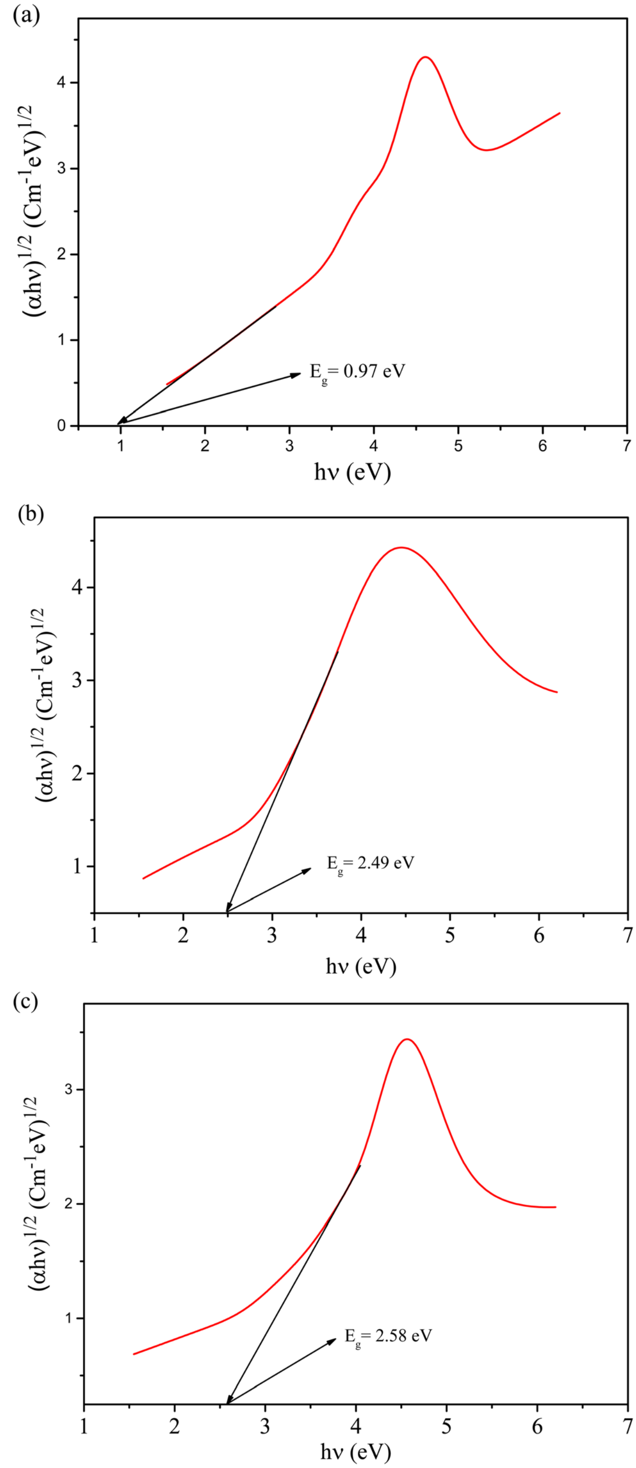

Fig. 6 Schematic illustration of band gap energies of (a) G, (b) AmI, and (c) GAL composite.

facilitate the adsorption of polar pharmaceuticals like AMX. Moreover, the electronic structure modification induced by composite formation creates a more stable adsorption environment, enabling both electrostatic interactions and π–π stacking between the composite's aromatic domains and the β-lactam structure of AMX.

3.6 Adsorption analysis

3.6.1 Effect of initial concentration and contact time. The study examined the adsorption of AMX onto a GAL composite at various initial concentrations (5, 10, 15, and 20 ppm) to assess how contact time affects adsorption efficiency.

Fig. 7 illustrates that both the adsorption capacity (Q_t, mg g^{-1}) and the percentage of removal increased significantly within the first 30 minutes, indicating rapid surface adsorption due to numerous active sites. This pattern aligns with previous research that reported swift initial adsorption because of the large surface area and functional groups available for interaction with amoxicillin.[24] After 40 minutes, the adsorption rate decreased, suggesting a gradual saturation of sites and the beginning of equilibrium. Equilibrium was achieved within 80–100 minutes, with minimal additional uptake beyond this period, similar to findings with activated carbon-based adsorbents.[46] Higher initial concentrations led to increased Q_t values, reaching approximately 96.02 mg g^{-1} for 20 ppm, while the percentage of removal was highest (98%) at lower concentrations (5 ppm) due to a greater ratio of active sites to solute molecules. This trend is consistent with studies showing an

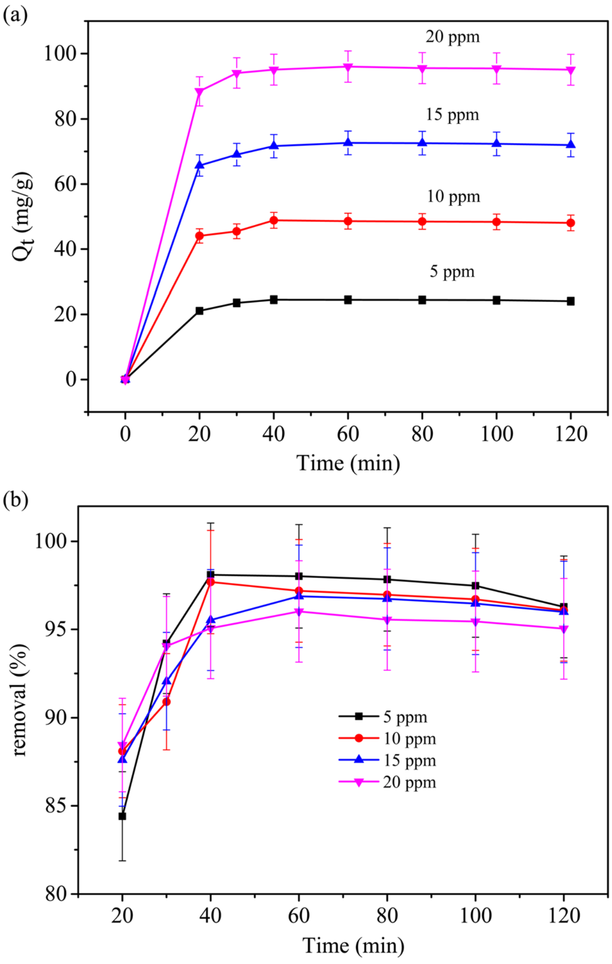

Fig. 7 Effect of contact time on (a) adsorption capacity (Q_t) and (b) removal% of AMX onto GAL composite at different initial concentrations (conditions: pH 6, adsorbent dosage 0.02 g, temperature 298 K).

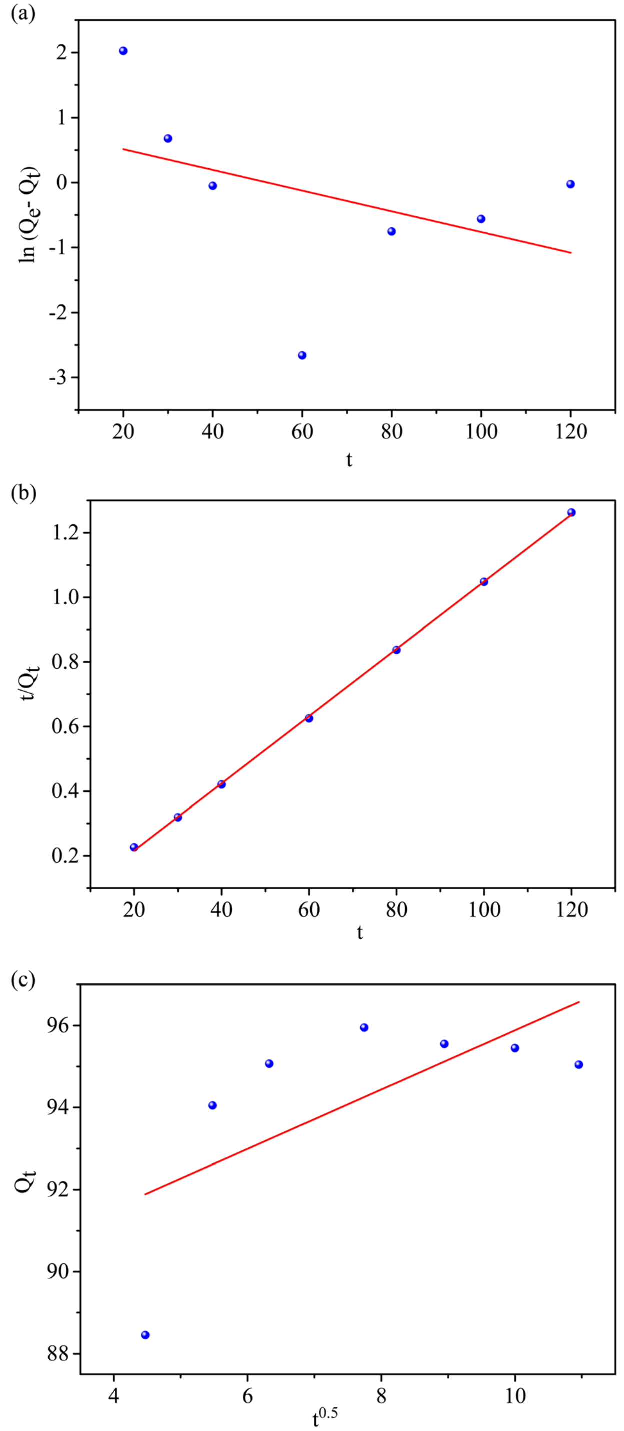

Fig. 8 Kinetic model for AMX adsorption onto GAL composite (a) pseudo first order (b) pseudo second order (c) intra-particular diffusion model.

inverse relationship between initial concentration and percentage of removal, where lower concentrations enable higher removal efficiency.[23] Despite differences in adsorption capacity, all concentrations showed a similar equilibrium time, underscoring the GAL composite's effectiveness in quickly removing amoxicillin. The observed patterns confirm that 80–100 minutes is the optimal contact time, ensuring both maximum adsorption efficiency and practical feasibility for wastewater treatment applications, making GAL composites a promising material for removing pharmaceutical pollutants.[40]

3.6.2 Adsorption kinetics. The adsorption kinetics of AMX onto the GAL composite were examined using pseudo-first-order, pseudo-second-order, and intra-particle diffusion models to elucidate the adsorption mechanism, as shown in Fig. 8. Table 1 represents the different kinetic parameters obtained for AMX adsorption. The pseudo-first-order model, which presumes physisorption, showed a poor fit with a low correlation coefficient ($R^2 = 0.173$), indicating that simple surface adsorption is not the primary controlling factor.[47] Conversely, the pseudo-second-order model demonstrated an excellent fit ($R^2 = 0.999$) value, with the calculated equilibrium adsorption capacity closely matching the experimental value, confirming that chemisorption governs the adsorption mechanism, involving electron sharing or exchange between AMX molecules and the GAL composite surface.[48,51,52] This behavior can be attributed to the presence of abundant functional groups from both graphene and aminated lignin, which facilitate strong interactions such as hydrogen bonding, electrostatic attraction, and π–π interactions.

Furthermore, the intra-particle diffusion model reveals a multi-linear relationship, indicating that adsorption proceeds through multiple sequential steps rather than a single rate-limiting mechanism. The initial sharp region corresponds to rapid external surface adsorption driven by the availability of abundant active sites and strong concentration gradients. This is followed by a gradual diffusion stage, where AMX molecules penetrate into the internal pores and interlayer spaces of the composite. Finally, a plateau region is observed, representing equilibrium conditions where adsorption slows due to site saturation. The non-zero intercept ($C \neq 0$) further confirms that intra-particle diffusion is not the sole rate-controlling step, and boundary layer diffusion also contributes significantly to the overall adsorption process.[26,53]

3.6.3 Adsorption isotherm study. The adsorption isotherm analysis provides critical insight into the interaction mechanism between AMX molecules and the GAL composite surface. In this study, the equilibrium data were analyzed using Langmuir, Freundlich, and Temkin isotherm models (Fig. 9 and Table 2). Among these, the Langmuir model exhibited the best fit with the highest correlation coefficient ($R^2 = 0.997$),

Table 1 Different kinetic parameters for the adsorption of AMX on GAL composite

Model	Parameter	Value
Pseudo 1st order	Q_e (mg g^{-1})	2.30
	k_1 (min^{-1})	0.016
	R^2	0.173
Pseudo 2nd order	Q_e (mg g^{-1})	96.15
	k_2 (g mg^{-1} min^{-1})	0.13
	R^2	0.999
Intra-particle diffusion	K_{diff} (mg g^{-1} $min^{-1/2}$)	0.723
	C	88.653
	R^2	0.442

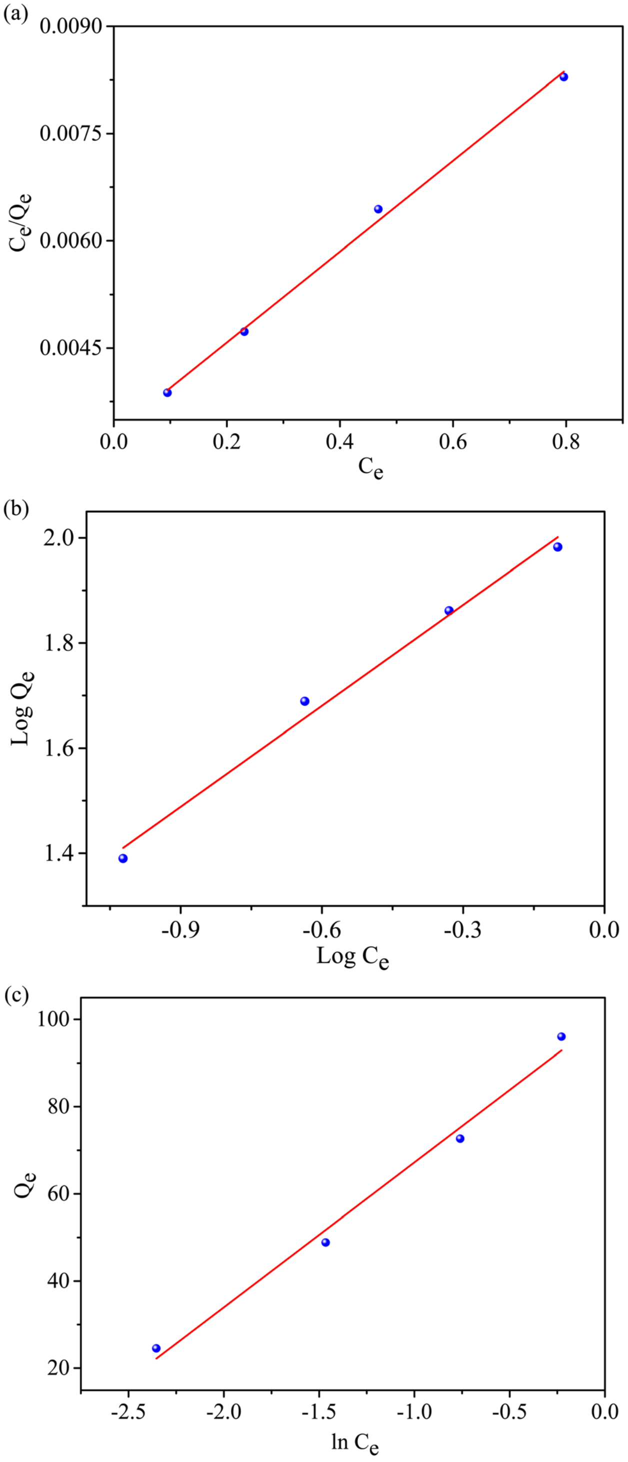

Fig. 9 Adsorption Isotherm of AMX from aqueous solution by GAL composite, (a) Langmuir isotherms, (b) Freundlich isotherms, and (c) Temkin model.

indicating that adsorption predominantly occurs as a monolayer on a homogeneous surface with a finite number of identical active sites.

The strong agreement with the Langmuir model suggests that the surface of the GAL composite provides energetically uniform adsorption sites, likely due to the well-dispersed graphene sheets and homogeneous distribution of aminated lignin functional groups. The high maximum adsorption capacity (Q_m = 156.25 mg g^{-1}) further confirms the strong affinity between AMX molecules and the composite surface. Similar Langmuir-dominated adsorption behavior has been reported for carbon-based and electrochemically derived adsorbents, where uniform active sites govern adsorption equilibrium.[18,54] Despite the dominance of the Langmuir model, the Freundlich model also exhibited a reasonably good fit (R^2 = 0.97), indicating the presence of surface heterogeneity and multilayer adsorption to some extent. The Freundlich constant (n = 1.59 > 1) confirms favorable adsorption conditions and suggests that adsorption intensity increases with surface coverage. This behavior is consistent with previous studies where heterogeneous adsorption arises from the distribution of functional groups and varying binding energies across the adsorbent surface.[49,55] However, the slightly lower R^2 value compared to the Langmuir model suggests that monolayer adsorption is the dominant process, similar to findings reported in graphene-based adsorbents.[18] Furthermore, the Temkin model provided additional insight into adsorbate–adsorbent interactions by considering the effect of indirect

Table 2 Different isotherm parameters for the adsorption of amoxicillin on GAL composite

Model	Parameter	Value
Langmuir	Q_m (mg g^{-1})	156.25
	K_L (L mg^{-1})	2
	R^2	0.997
Freundlich	n	1.59
	K_f (mg g^{-1})	7.85
	R^2	0.97
Temkin	B_t (kJ mol^{-1})	32.8
	K_t (L mg^{-1})	21.23
	R^2	0.98

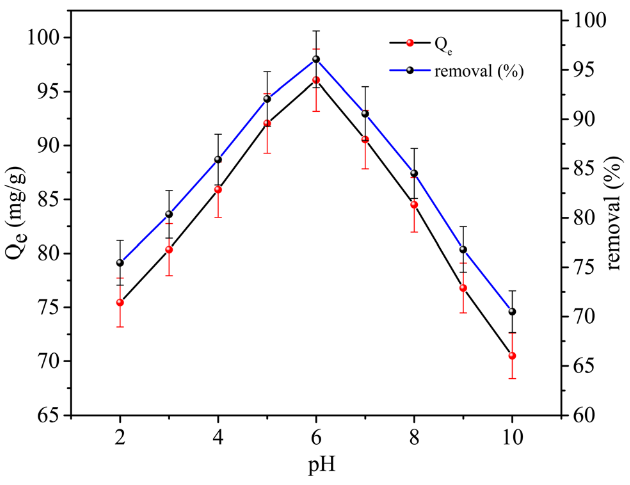

Fig. 10 Effect of pH on AMX adsorption by GAL composite (conditions: initial concentration 20 mg L^{-1}, adsorbent dosage 0.02 g, contact time 60 min, temperature 298 K).

adsorbate interactions on adsorption energy. The moderate correlation coefficient ($R^2 = 0.98$) indicates that the heat of adsorption decreases linearly with increasing surface coverage, suggesting that adsorbate–adsorbent interactions weaken as active sites become occupied. Such behavior has been widely observed in adsorption systems involving organic pollutants, where interaction energy gradually decreases due to site saturation.[47,56]

3.6.4 Effect of pH. Fig. 10 reveals that the adsorption of AMX onto the GAL composite is significantly influenced by pH levels, with the highest adsorption occurring at pH 6. At lower pH levels (2–4), both the adsorbent surface and AMX molecules become protonated, resulting in electrostatic repulsion and decreased adsorption. This phenomenon is consistent with studies indicating that acidic conditions impede adsorption due to strong repulsive forces between positively charged functional groups on the adsorbent and cationic AMX species.[1] As the pH approaches neutrality, AMX takes on a zwitterionic form, which enhances interactions with the composite surface and optimizes adsorption efficiency. Beyond pH 6, adsorption diminishes due to the deprotonation of functional groups on both the AMX molecule and the GAL composite, causing electrostatic repulsion between negatively charged species. Similar patterns have been observed in research on pH-dependent adsorption mechanisms in graphene-based materials.[23] In alkaline conditions (pH 8–10), competition with hydroxyl ions further diminishes adsorption efficiency by reducing available active sites and encouraging desorption. The findings confirm that electrostatic interactions and molecular speciation are key factors in the adsorption process. Optimal removal is achieved at a pH of 6, highlighting its importance in wastewater treatment.[50]

3.6.5 Effect of adsorbent dosages. The adsorption of AMX onto the GAL composite is also greatly affected by the adsorbent dosage, as displayed in Fig. 11. At lower dosages (0.010–0.015 g), the adsorption capacity (Q_t) is high due to a higher ratio of active sites to AMX molecules. However, as the dosage increases beyond 0.015 g, Q_t decreases because of adsorbent aggregation, which reduces the available surface area and impairs adsorption efficiency.[25] Conversely, the percentage removal of AMX rises with higher dosages, exceeding 95% at 0.020 g and above. This trend occurs because more adsorption sites are available to capture AMX molecules, similar to findings in lignin-based adsorbents.[24] However, beyond a specific dosage, the removal percentage levels off, indicating that adding more adsorbent does not significantly enhance performance. This behavior is consistent with previous studies showing that excessive adsorbent dosage leads to inefficient use of active sites.[49]

3.6.6 Effect of temperature. Fig. 12 exposed that the study examined how temperature affects the adsorption of AMX onto a GAL composite, within a temperature range of 298 to 313 K. As the temperature increased, both parameters showed a steady rise, indicating improved adsorption performance at higher temperatures. Specifically, the adsorption capacity rose from 95.52 mg g^{-1} at 298 K to 97.40 mg g^{-1} at 313 K, and the percentage removal increased from 95.52% to 97.40%. This pattern suggests that the adsorption process is endothermic, likely due to increased molecular mobility and enhanced diffusion of AMX molecules towards the active sites on the GAL composite at higher temperatures. The endothermic nature of the process implies stronger interactions between AMX molecules and the GAL surface, potentially involving chemisorption mechanisms such as hydrogen bonding, electrostatic interactions, or π–π electron donor–acceptor interactions. These results align with previous studies indicating that higher temperatures enhance the uptake of pharmaceutical compounds by carbonaceous adsorbents due to pore volume expansion and activation of functional groups on the adsorbent surface. Furthermore, the increase in adsorption capacity with temperature supports the hypothesis that the adsorption process is influenced not only by physical forces but also by

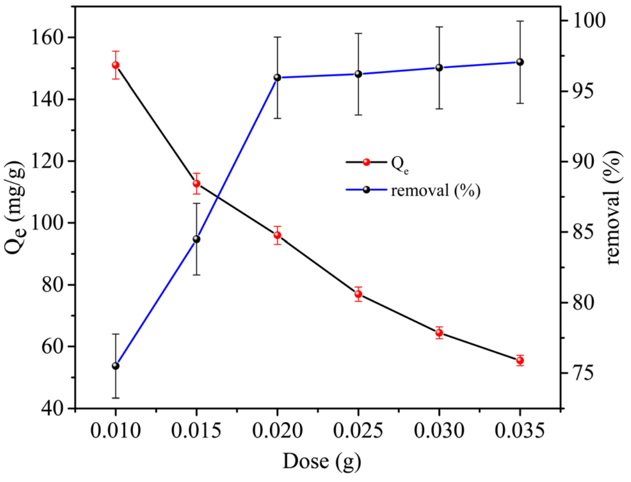

Fig. 11 Effect of adsorbent dosages on AMX adsorption by GAL composite (conditions: initial concentration 20 mg L^{-1}, pH 6, contact time 60 min, temperature 298 K).

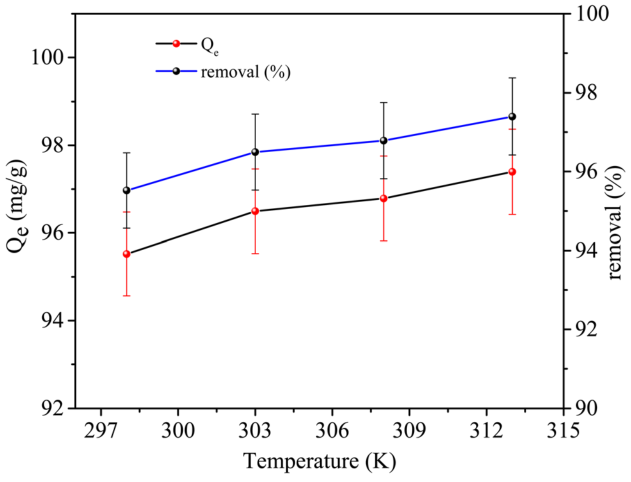

Fig. 12 Effect of temperature on amoxicillin adsorption by GAL composite (conditions: initial concentration 20 mg L^{-1}, pH 6, adsorbent dosage 0.02 g, contact time 60 min).

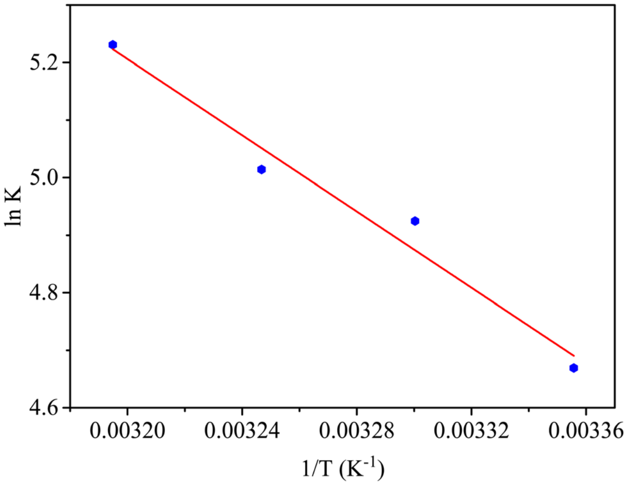

Fig. 13 Thermodynamics study on AMX adsorption by GAL composite.

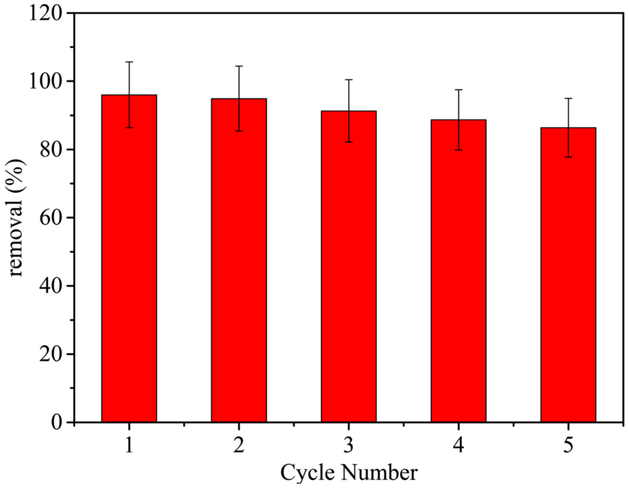

Fig. 14 Reusability of GAL composite on AMX adsorption from aqueous solution (conditions: initial concentration 20 mg L^{-1}, pH 6, adsorbent dosage 0.02 g, contact time 60 min, temperature 298 K).

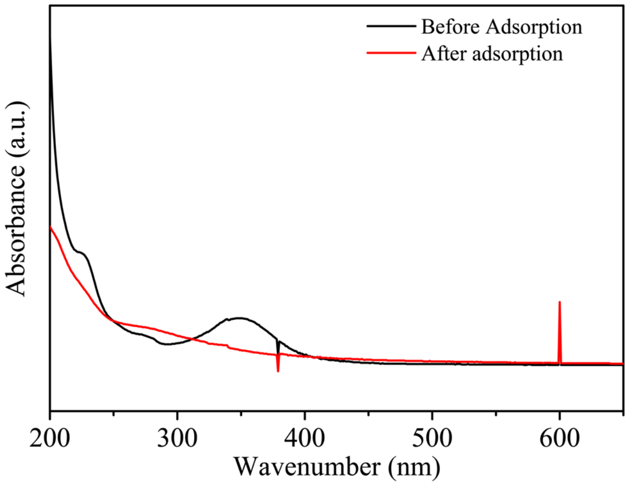

Fig. 15 UV-Vis spectra of AMX solution before and after adsorption.

chemical interactions, which are more favorable at higher thermal energy levels.[57]

3.6.7 Thermodynamic study. To clarify the characteristics of AMX adsorption on the GAL composite, thermodynamic parameters were assessed using the van't Hoff equation. The linear graph of ln K against $1/T$ (Fig. 13) produced a slope of −3311.8 and an intercept of 15.8, from which the standard enthalpy ($\Delta H°$) and entropy ($\Delta S°$) changes were determined to be +27.53 kJ mol^{-1} and +0.131 J mol^{-1} K^{-1}, respectively. The positive $\Delta H°$ indicates that the adsorption process is endothermic, implying that higher temperatures enhance the interaction between AMX molecules and GAL active sites.[58,59] The positive $\Delta S°$ suggests increased disorder at the solid–liquid interface, likely due to the displacement of water molecules and structural rearrangement of AMX during adsorption.[60,61] The Gibbs free energy change ($\Delta G°$) values were negative across all temperatures studied, ranging from −11.59 to −13.56 kJ mol^{-1}, indicating that the adsorption process is spontaneous and thermodynamically favorable.[62] Furthermore, the increasingly hostile $\Delta G°$ with rising temperature supports a stronger driving force for adsorption at higher temperatures (Table 3).

3.6.8 Reusability. The ability of the GAL composite to be reused for removing AMX was assessed through five cycles of adsorption and desorption. Fig. 14 illustrates a gradual decline in removal efficiency, starting from nearly 96.02% in the initial cycle to about 86.4% by the fifth cycle. This reduction is likely attributed to the partial deactivation of active sites and the structural breakdown of the adsorbent. Similar patterns have been noted in adsorbents based on graphene and lignin, where the loss of functional groups and pore blockage lead to diminished adsorption capacity.[63,64] Despite this, the material maintains considerable efficiency after several cycles, indicating its potential for practical wastewater treatment applications. Implementing effective regeneration methods, such as chemical washing or thermal treatment, could further improve its long-term reusability.[24]

Table 3 Thermodynamic parameters obtained for the adsorption process of AMX using GAL composite

	$\Delta S°$ (J mol^{-1})	$\Delta H°$ (kJ mol^{-1})	$-\Delta G°$ (kJ mol^{-1})			
			298	303	308	313
AMX	131.36	27.53	11.59	12.24	12.9	13.56

3.6.9 Adsorption mechanism. The adsorption of AMX onto the GAL composite proceeds through a synergistic multi-interaction mechanism involving π–π stacking, hydrogen bonding, electrostatic attraction, and chemisorption. The extended π-conjugated domains of graphene enable strong π–π interactions with the aromatic rings of AMX, facilitating rapid initial uptake, while the aminated lignin component provides abundant $-NH_2$, –OH, and residual oxygenated functional groups that form stable hydrogen bonds with the β-lactam

Table 4 Comparative analysis of different types of adsorbents on AMX adsorption

Adsorbent	Adsorbate	Adsorption capacity	Reference
MnO_2@carbon microspheres	AMX	16.094	23
Hydroxyl-functionalized graphene	AMX	59.5	3
Magnetic graphene nanoplatelets	AMX	14.1	
Magnetic graphene oxide	AMX	98.41	
GO/Poly(CMC-*co*-AA)	AMX	12.486	2
Kaolinite clay	AMX	12	63
GAL composite	AMX	96.02	Present work

carbonyl, amide, and hydroxyl groups of AMX, as supported by UV-Vis spectral changes.[65] Electrostatic interactions play a crucial pH-dependent role, with optimal adsorption at pH 6, where AMX exists predominantly in a zwitterionic form, and the GAL surface carries partially protonated amine groups, minimizing repulsion and enhancing attraction.[66] The excellent agreement with the pseudo-second-order kinetic model confirms that chemisorption, involving electron sharing or exchange between AMX molecules and active sites on the GAL surface, governs the adsorption rate, while the positive enthalpy change ($\Delta H° = 27.53$ kJ mol^{-1}) indicates an endothermic process driven by strong specific interactions. Langmuir isotherm fitting suggests monolayer adsorption on a relatively homogeneous surface, enabled by the uniform dispersion of aminated lignin within the graphene framework, which suppresses aggregation and increases site accessibility. Intraparticle diffusion analysis further reveals a multistep process consisting of rapid surface adsorption followed by gradual diffusion into internal pores and interlayer regions, culminating in equilibrium saturation.

3.6.10 UV-Vis spectroscopic analysis. The UV-Vis spectra of AMX solution before and after adsorption onto the GAL composite are shown in Fig. 15. The pristine amoxicillin solution exhibited a pronounced absorption band at 230 nm, corresponding to the $\pi \rightarrow \pi^*$ transition of the aromatic ring and β-lactam carbonyl chromophores of the amoxicillin molecule.[67] A minor shoulder around 272 nm (often faint in diluted solutions) arises from transitions within the aromatic substituents attached to the benzene ring.

After adsorption onto the GAL composite, a substantial reduction in absorbance intensity was observed across the UV region, confirming the effective removal of amoxicillin from the aqueous phase. The decrease in peak intensity at 230 nm indicates the depletion of the chromophoric species due to adsorption. In addition, the absence of any new absorption peaks after adsorption suggests that no degradation or structural modification of amoxicillin occurred during the process, implying a physical adsorption mechanism rather than photochemical decomposition.

The adsorption efficiency can be attributed to multiple interactions between amoxicillin and the GAL surface. The π-conjugated domains of graphene facilitate π–π stacking interactions with the aromatic moieties of amoxicillin, while the amine groups of lignin contribute electrostatic attraction and hydrogen bonding with the carboxyl and amide groups of the antibiotic. These synergistic effects enhance molecular affinity, leading to the observed decline in absorbance intensity.

4. Conclusion

This study highlights the transformative potential of the GAL composite as an advanced adsorbent for effectively removing AMX from water systems. The GAL composite not only showed an impressive adsorption capacity of 96.02 mg g^{-1} but also exhibited superior kinetic behavior, aligning with pseudo-second-order dynamics, and favorable thermodynamic properties, spontaneous ($\Delta G < 0$) and endothermic ($\Delta H = 27.53$ kJ mol^{-1}). The best adsorption occurred at pH 6, driven by a combination of π–π interactions, hydrogen bonding, and electrostatic attractions. Additionally, the material's regeneration efficiency remained strong (86.4%) over five cycles, underscoring its practical viability and cost-effectiveness for repeated use. By leveraging the inherent properties of lignin and the high surface area of graphene, this composite represents a fusion of green chemistry and nanotechnology, addressing a significant environmental issue with a scalable, economical, and environmentally friendly solution. This work makes a substantial contribution to the field of sustainable water purification, providing a versatile platform for removing pharmaceutical contaminants with industrial and ecological significance (Table 4).[68,69]

Author contributions

Riyadh Hossen Bhuiyan: conceptualization, supervision, investigation, methodology, formal analysis, data analysis, writing – original draft and editing; Md. Masum Billah: investigation, methodology, formal analysis, data analysis, writing – original draft and editing; Mohammad Mahbubur Rahman: validation, funding acquisition, writing – review and editing; Swapan Kumer Ray: supervision, validation, funding acquisition, writing – review and editing; Monira Binte Mesbah: formal analysis, writing – reviewing and editing; Satyajit Roy Rony: formal analysis, writing – reviewing and editing; Md. Sahadat Hossain: methodology, supervision, investigation, formal analysis, writing – reviewing and editing; Md. Shohidul Islam: formal analysis, writing, reviewing, and editing, Md. Kamrul Hasan Dipu: methodology, investigation, formal analysis, writing – reviewing and editing; Zahidul Islam: investigation, formal analysis, writing – reviewing and editing; Mohammad Amirul Hoque: conceptualization, validation, funding acquisition, writing – review and editing.

Conflicts of interest

The authors state that there are no conflicts of interest, financial, commercial, or personal relationships associated with this research.

Data availability

The data supporting the findings of this study are available from the corresponding author upon reasonable request.

Acknowledgements

The authors acknowledge the Bangladesh Council of Scientific and Industrial Research and Gopalganj Science and Technology University, Gopalganj, Dhaka, for their support of this work.

References

1 A. Kaur and C. Maity, *J. Phys.: Conf. Ser.*, 2020, **1531**, 012109.
2 M. A. Awad and L. S. Jasim, *Qual. Assur.*, 2021, **12**, 88–94.
3 J. C. S. Aguilar, C. P. Lawagon, J. M. M. Gallawan and J. G. Cabotaje, *Chem. Eng. Trans.*, 2021, **86**, 331–336.
4 J. O. Eniola, R. Kumar and M. A. Barakat, *Environ. Sci. Pollut. Res.*, 2019, **26**, 34775–34788.
5 R. Kamaraj, N. Nesakumar and S. Vasudevan, *ChemistrySelect*, 2020, **5**, 10034–10040.
6 R. Kamaraj and S. Vasudevan, *ChemistrySelect*, 2019, **4**, 2428–2435.
7 P. Aarthi, R. Kamaraj and S. Vasudevan, *New J. Chem.*, 2017, **41**, 4518–4530.
8 R. Kamaraj and S. Vasudevan, *New J. Chem.*, 2016, **40**, 2249–2258.
9 J. M. Chaba and P. N. Nomngongo, *Emerging Contam.*, 2019, **5**, 143–149.
10 B. Muthukutty, J. Ganesamurthi, S. M. Chen, B. Arumugam, F. M. Chang, S. M. Wabaidur, Z. A. AlOthman, T. Altalhi and M. A. Ali, *Electrochim. Acta*, 2021, **386**, 138482.
11 J. Ganesamurthi, R. Shanmugam, T.-W. Chen, S.-M. Chen, M. Balamurugan, Z.-W. Gan, M. R. Siddiqui, S. M. Wabaidur and M. A. Ali, *Colloids Surf., A*, 2022, **647**, 129077.
12 F. Yu, Y. Li, S. Han and J. Ma, *Chemosphere*, 2016, **153**, 365–385.
13 I. H. Alsohaimi, S. M. Wabaidur, M. Kumar, M. A. Khan, Z. A. Alothman and M. A. Abdalla, *Chem. Eng. J.*, 2015, **270**, 9–21.
14 X. Su, T. Xu, R. Ye, C. Guo, S. M. Wabaidur, D.-L. Chen, S. Aftab, Y. Zhong and Y. Hu, *J. Colloid Interface Sci.*, 2023, **646**, 129–140.
15 J. Sengupta and C. M. Hussain, *C*, 2024, **10**, 92.
16 M. Li, Y. Liu, G. Zeng, N. Liu and S. Liu, *Chemosphere*, 2019, **226**, 360–380.
17 Z. Wu, W. Huang, X. Shan and Z. Li, *Int. J. Biol. Macromol.*, 2020, **143**, 325–333.
18 M. M. Billah, S. P. Shandhi, M. R. Naim, M. B. Mesbah, S. A. Eti, M. Kamruzzaman and M. A. Hoque, *Surf. Interfaces*, 2025, **74**, 107655, DOI: 10.1016/j.surfin.2025.107655.
19 Z. Yan, T. Wu, G. Fang, M. Ran, K. Shen and G. Liao, *RSC Adv.*, 2021, **11**, 4713–4722.
20 T. R. Brazil, *et al.*, *Water*, 2024, **16**, 1838.
21 J. Ma, Z. Jiang, J. Cao and F. Yu, *Chemosphere*, 2020, **242**, 125188.
22 P. Bahar, A. H. Hassani, H. A. Panahi and E. Moniri, *Desalin. Water Treat.*, 2021, **210**, 281–295.
23 O. K. Taghzouti, K. El Mabrouk, M. Bricha and K. Nouneh, *SN Appl. Sci.*, 2019, **1**, 226.
24 L. Ren, D. Zhou, J. Wang, T. Zhang, Y. Peng and G. Chen, *J. Mol. Liq.*, 2020, **309**, 113074.
25 S. Tahmasebi, O. Moradi and M. Yari, *Int. J. Nano Dimens.*, 2016, **7**, 144–149.
26 S. X. Zha, Y. Zhou, X. Jin and Z. Chen, *J. Environ. Manage.*, 2013, **129**, 569–576.
27 A. Mohammadi, M. Kazemipour, H. Ranjbar, R. B. Walker and M. Ansari, *Fullerenes, Nanotub. Carbon Nanostruct.*, 2015, **23**, 165–169.
28 Z. Wu, X. Zhao, J. Zhang, X. Li, Y. Zhang and F. Wang, *Bioresour. Technol.*, 2019, **278**, 187–194.
29 L. Shao, *et al.*, *Mater. Des.*, 2016, **99**, 235–242.
30 Z. A. Alothman, A. H. Bahkali, M. A. Khiyami, S. M. Alfadul, S. M. Wabaidur, M. Alam and B. Z. Alfarhan, *Sep. Sci. Technol.*, 2020, **55**, 1766–1775.
31 N. F. Al-Harby, E. F. Albahly and N. A. Mohamed, *Polymers*, 2021, **13**, 4446.
32 J. Liu and X. Wang, *Sci. World J.*, 2013, **2013**, 897159.
33 X. Deng, L. Lü, H. Li and F. Luo, *J. Hazard. Mater.*, 2010, **183**, 923–930.
34 E. R. Kenawy, A. A. Ghfar, S. M. Wabaidur, M. A. Khan, M. R. Siddiqui, Z. A. Alothman, A. A. Alqadami and M. Hamid, *J. Environ. Manage.*, 2018, **219**, 285–293.
35 S. Kubo and J. F. Kadla, *Biomacromolecules*, 2005, **6**, 2815–2821.
36 A. Ali, M. I. Vohra, A. Nadeem, B. S. Al-Anzi, M. Iqbal, A. A. Memon, K. H. Thebo, *et al.*, *ACS Appl. Polym. Mater.*, 2024, **6**, 4747–4755.
37 Q. Lian, *et al.*, *Chemosphere*, 2021, **280**, 130730.
38 T. Shi, *et al.*, *Green Chem.*, 2022, **24**, 9040–9054.
39 R. H. Bhuiyan, *et al.*, *RSC Adv.*, 2026, **16**, 2093–2111.
40 H. Pan, G. Sun and T. Zhao, *Int. J. Biol. Macromol.*, 2013, **59**, 221–226.
41 Q. Zheng, G. Nong and N. Li, *Polymers*, 2024, **16**, 1237.
42 H. Chen, T. Liu, Y. Meng, Y. Cheng, J. Lu and H. Wang, *Colloids Surf., A*, 2020, **603**, 125281.
43 Z. Yu, F. Nan, L. Su, S. Zhang and Y. He, *J. Nanomater.*, 2019, **2019**, 5290496.
44 B. Du, *et al.*, *Sep. Purif. Technol.*, 2022, **297**, 121509.
45 B. Gürünlü, Ç. T. Yücedağ and M. R. Bayramoğlu, *J. Nanomater.*, 2020, **2020**, 7029601.

46 S. Nikafshar, O. Zabihi, Y. Moradi, M. Ahmadi, S. Amiri and M. Naebe, *Polymers*, 2017, **9**, 266.

47 H. Zhang, X. Zhang, L. Wang, B. Wang, X. Zeng, B. Ren and X. Yang, *ACS Omega*, 2023, **8**, 2435–2444.

48 Z. Çiplak, N. Yildiz and A. Çalimli, *Fullerenes, Nanotub. Carbon Nanostruct.*, 2015, **23**, 361–370.

49 A. Skulcova, V. Majova, M. Kohutova, M. Grosik, J. Sima and M. Jablonsky, *BioResources*, 2017, **12**, 6713–6722.

50 A. Khan, V. Nair, J. C. Colmenares and R. Gläser, *Top. Curr. Chem.*, 2018, **376**, 20.

51 A. A. Castellanos-Gomez and B. J. van Wees, *Graphene*, 2013, **2**, 102–108.

52 K. M. Samb-Joshi, Y. A. Sethi, A. A. Ambalkar, H. B. Sonawane, S. P. Rasale, R. P. Panmand, M. G. Chaskar, *et al.*, *J. Compos. Sci.*, 2019, **3**, 90.

53 A. Pandiarajan, R. Kamaraj, S. Vasudevan and S. Vasudevan, *Bioresour. Technol.*, 2018, **261**, 329–341.

54 R. Kamaraj and S. Vasudevan, *Res. Chem. Intermed.*, 2016, **42**, 4077–4095.

55 R. Kamaraj, A. Pandiarajan, S. Jayakiruba, M. Naushad and S. Vasudevan, *J. Mol. Liq.*, 2016, **215**, 204–211.

56 R. Kamaraj, D. J. Davidson, G. Sozhan and S. Vasudevan, *RSC Adv.*, 2015, **5**, 39799–39809.

57 P. Ganesan, J. Lakshmi, G. Sozhan and S. Vasudevan, *Can. J. Chem. Eng.*, 2013, **91**, 448–458.

58 S. Vasudevan, J. Lakshmi and G. Sozhan, *Water Environ. Res.*, 2012, **84**, 209–219.

59 A. M. Aljeboree, A. N. Alshirifi and A. F. Alkaim, *Plant Arch.*, 2019, **19**, 915–919.

60 L. Limousy, I. Ghouma, A. Ouederni and M. Jeguirim, *Environ. Sci. Pollut. Res.*, 2017, **24**, 9993–10004.

61 S. Vasudevan, J. Jayaraj, J. Lakshmi and G. Sozhan, *Korean J. Chem. Eng.*, 2009, **26**, 1058–1064.

62 I. P. Oyekunle, *et al.*, *J. Water Process Eng.*, 2025, **70**, 106936.

63 S. Vasudevan, J. Lakshmi and G. Sozhan, *Desalin. Water Treat.*, 2009, **12**, 407–414.

64 S. Jellali, *et al.*, *Processes*, 2024, **12**, 1552.

65 L. El Azzouzi, S. El Aggadi, M. Ennouhi, A. Ennouari, O. K. Kabbaj and A. Zrineh, *Sci. Afr.*, 2022, **18**, e01390.

66 B. H. Alshammari, *et al.*, *RSC Adv.*, 2024, **14**, 5875–5892.

67 N. Dolfini, C. M. B. D. Araujo and N. C. Pereira, *Environ. Technol.*, 2024, **45**, 1636–1650.

68 Ö. Kerkez-Kuyumcu, Ş. S. Bayazit and M. A. Salam, *J. Ind. Eng. Chem.*, 2016, **36**, 198–205.

69 F. K. Mostafapour, M. Bazi, S. H. Siddiqui, H. Bagheri and D. Balarak, *Int. J. Pharm. Investig.*, 2021, **11**, 384–388.